Chirping Ion Cyclotron Emission (ICE) on NSTX-U

E. D. Fredrickson, N. N. Gorelenkov, R. E. Bell, A. Diallo, B. P. LeBlanc, J. Lestz, M. Podestà and the NSTX team

Princeton Plasma Physics Laboratory, Princeton New Jersey 08543

eric@pppl.gov

Abstract.

We report here on the discovery on NSTX-U of a qualitatively new type of non-thermal emission from plasmas in the ion-cyclotron frequency range (ICE). This new type of ICE is weakly damped, $\gamma_{\text{damp}}/\omega_{ICE} \approx 0.14\%$, low order eigenmodes, excited by a fast ion population radially located near an internal transport barrier. The ICE appears as repetitive bursts with durations of ≈ 1 ms, and the bursts exhibit frequency chirps upwards and/or downwards with maximum $\delta f/f \approx 1\%$. We refer to this chirping ICE as ch-ICE. The bursts are longer than the typical ICE bursts of $\approx 100 \ \mu s$ reported previously for NSTX and NSTX-U, for simplicity, NSTX(-U). The chirping resembles that seen in modeling of weakly unstable fast particle driven instabilities [cf., Berk, et al., Phys. Lett. A 234, (1997) 213]. These data also provide some preliminary indications of non-linear coupling between the ch-ICE harmonics. extensive experimental and theoretical studies of ICE, theoretical understanding of ICE remains qualitative at best. The detailed experimental observations of ICE from NSTX(-U) find a wide variation in the ICE characteristics. The new observations of ch-ICE presented here, combined with the characteristics of ICE on NSTX(-U) previously reported [Fredrickson, et al., Phys. Plasmas 26 (2019), 032111], could guide the development of more complete theoretical models of ICE.

Keywords: ICE, energetic particles, NSTX, NSTX-U

I. Introduction

Super-thermal electromagnetic emission from laboratory plasmas in the ion-cyclotron frequency range, commonly referred to as ion cyclotron emission or ICE, has been extensively studied, both to understand the phenomena and as a potential diagnostic of the confined fast ion populations in fusion plasmas [1-29]. Present theoretical models of ICE are qualitative at best and interpretations of ICE as compressional Alfvén waves or the magneto-acoustic instability [28-45], mode-converted ion Bernstein waves [46] or even spin-flip maser emission [47] have been proposed. The ICE frequency is in general close to the cyclotron frequency of a superthermal energetic ion population located near the plasma outboard edge, although ICE has been seen in ohmic and beam heated plasmas with frequencies corresponding to the ion cyclotron frequency near the axis [4,16,17,18,19,26-29]. The ICE is believed to be excited through a cyclotron resonance with this super-thermal fast ion population with the resonant frequency Doppler-shifted from the cyclotron frequency by $k_{\parallel}V_{\parallel}$ where k_{\parallel} and V_{\parallel} are the components of the wave vector and the energetic-ion velocity parallel to the magnetic field, respectively. This poses an additional complication for NSTX(-U) and other spherical tokamaks as the ion cyclotron frequency is relatively low compared to the potentially large Doppler-shift expected from 70 - 90 keV beam ions. Thus in spherical tokamaks the ICE frequency could be significantly shifted from the cyclotron frequency at the resonance location.

The possibility that ICE could serve as a diagnostic of the confined fast-ion population in ignited plasmas such as are expected for ITER [43-45] has renewed interest in developing a comprehensive theoretical model of ICE. The environment for diagnostics on ITER is challenging, but ICE can be measured with a small coil or with the Ion-Cyclotron Range of Frequency (ICRF) antennas. Relating the measured ICE frequency and intensity to parameters of the confined fast ion population, however, will require an improved theoretical understanding of ICE. The unique characteristics of ICE on NSTX(-U) could help steer research towards more complete theoretical models.

Four qualitatively different types of ICE have been identified on NSTX(-U). All of the ICE types are observed to be coherent, global modes and the width of the frequency peaks of the ICE is narrow with $\delta f/f \leq 0.1$ %. The first and most commonly seen type of ICE has many similarities to the observations of ICE on conventional aspect ratio tokamaks. This ICE appears in bursts lasting $\approx 100~\mu s$ [5,9,25] and emission has been seen in bands near harmonics of the deuterium ion cyclotron frequency (Ω_D) up to the seventh. NSTX(-U) operates with nominally deuterium plasmas with deuterium neutral beam heating. As previously reported, multiple discrete frequencies are typically seen at each harmonic [9,19,25]. The second type is very similar to the first, except that the ICE appears in a quasi-stationary state with moderate amplitude modulation, but no bursting. The quasi-stationary character of the ICE allowed

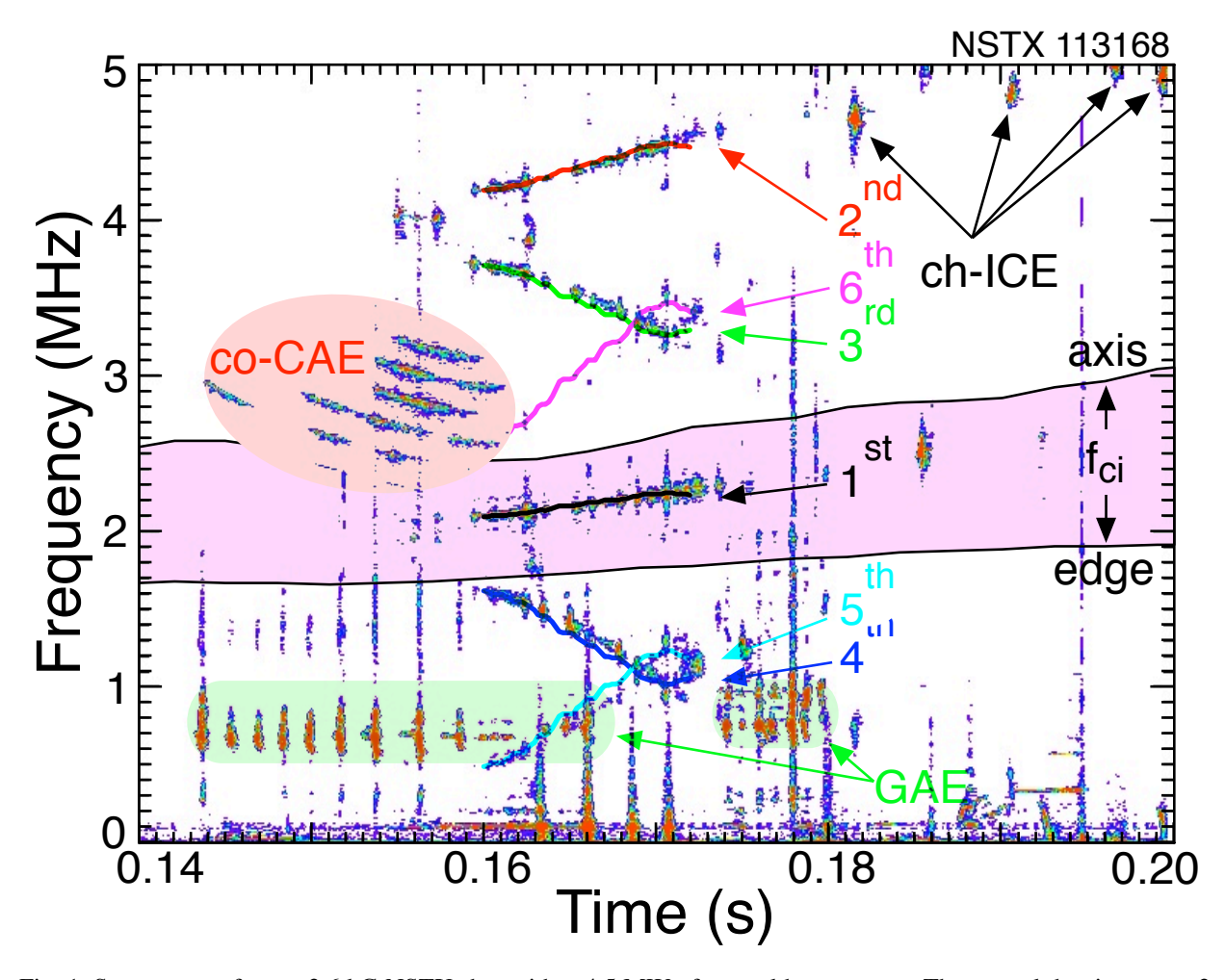


Fig. 1. Spectrogram from a 2.6 kG NSTX shot with \approx 4.5 MW of neutral beam power. The central density was < 2 x 10^{13} /cm³, $T_e \approx 0.8$ keV. The range of deuterium cyclotron frequency between plasma edge and axis is shaded magenta. GAE avalanches are seen in green-shaded region. Co-propagating CAE with $10 \le n \le 15$ are in redshaded region. The 1st through 5th harmonics of ICE and ch-ICE bursts are as indicated.

observation of three-wave coupling between the ICE and lower frequency Global Alfvén eigenmodes [25]. The third type is also bursting with bursts lasting ≈ 1 ms, but the frequency during the bursts changes (chirps) by up to ≥ 200 kHz ($\delta f/f \leq 1$ %). This chirping ICE, which we refer to here as ch-ICE, has not been seen at Ω_D and has not been previously reported. (A different type of "chirping" ICE has been reported from KSTAR where the chirps are the result of density changes in filaments during the collapse of ELMs [18,23,24].) A fourth type, only seen in a few shots, is a weaker, bursting ICE that appears to originate from a magnetic well in high current, low field and high β plasmas. The bursts of this fourth type of ICE were short ($\approx 10~\mu$ s) and again, narrow band, but scattered over a range of frequencies that encompasses the cyclotron frequencies in the magnetic well. An important unique characteristic of the first three types of ICE on NSTX(-U) is that the ICE frequency is higher than the cyclotron frequency at the plasma edge suggesting that the ICE originates from deeper in the plasma [25].

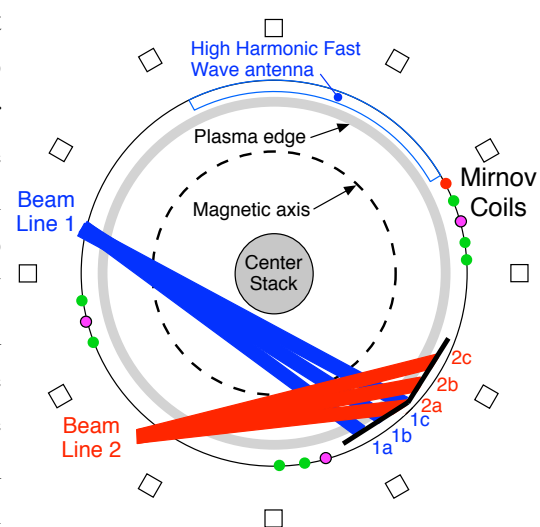
As the modes are typically measured to be counter-propagating, present theoretical models would predict that the Doppler shifted ICE frequency should be *lower* than the edge cyclotron frequency. ICE with frequency higher than the edge cyclotron frequency is also predicted to damp on the thermal deuterium plasma. In this paper we will present the new data on the third type of ICE, the chirping ICE, which was not discussed in our earlier publication [25].

Most theoretical models assume that the ICE is the fast, or compressional, Alfvén wave and it is important to note that the ICE behaves qualitatively differently from the co-propagating CAE previously reported on NSTX [48, 49]. Figure 1 shows a spectrogram of magnetic fluctuations during a 2.6 kG NSTX shot heated with 4.5 MW of NBI. The spectrogram is complicated, but includes co-propagating CAE, Global Alfvén eigenmodes (GAE), and examples of the first and third types of ICE. The deuterium cyclotron frequency in the region from the plasma edge to the magnetic axis is highlighted in magenta. As indicated by the pink region in the figure, the co-CAE appear between roughly 0.14 s and 0.16 s with frequencies between 2.5 MHz and 3.5 MHz, a frequency higher than even Ω_D at the magnetic axis. The GAE, green high-lighted regions, are bursting and chirping with frequency below 1 MHz, and with weak 2nd harmonics visible. The ICE appears between 0.16 s and 0.175 s, with the fundamental frequency between 2.2 MHz and 2.4 MHz (the third through sixth harmonics are aliased). Some scattered bursts of ch-ICE appear after 0.18 s (where the chirping is not visible on this scale). In this figure it is seen that the ICE is clearly qualitatively different than the co-CAE, nor is ICE the counterpropagating CAE [50] which typically have frequencies less than half the edge Ω_D (and are not present in this shot).

The ch-ICE has a number of characteristics that distinguish it from the typical ICE. The frequency of ch-ICE at each harmonic is slightly lower than the harmonics of the first, or "typical", type of ICE, and ch-ICE has only been seen at the second through sixth harmonics of the Ω_D (most commonly, but not exclusively, at the even harmonics). In Sect. II we describe the experiment conditions and in Sect. III we present experimental data illustrating some specific characteristics of the ch-ICE. In Sect. IV we will describe in more detail the chirping of ch-ICE, a unique feature of this type of ICE, with possible implications regarding the instability drive for ch-ICE. In Sect. V we will discuss measurements of the mode structure, specifically toroidal mode numbers, direction of mode propagation and local poloidal wavelength measurements on the outboard mid-plane. Section VI will describe some evidence for non-linear coupling between the ICE harmonics. Section VII will discuss the implications of the experimental observations and Section VIII will summarize the results and discuss needs and plans for further research.

II. Experimental Setup

The National Spherical Tokamak eXperiment Upgrade (NSTX-U) [51, 52] is a tight aspect ratio tokamak with a major radius of ≈ 0.94 m and minor radius of ≈ 0.55 m. NSTX-U is an upgrade of the NSTX with a larger diameter "center stack" which Beam allows higher field (up to 1 Tesla), plasma current up to 2 MA, and pulse lengths as long as 5 s. NSTX-U also has three additional deuterium neutral beam sources with the new sources aimed at the outer edge of the plasma (red beam trajectories in Fig. 2). The examples of ch-ICE shown in this paper come from both NSTX and NSTX-U plasmas with nominal toroidal fields ranging from 2.6 kG up to the highest Fig. 2. Plan-view of NSTX-U at the mid-plane. achieved field to date of 5.9 kG. Thomson scattering measurements of the electron temperature and mounted. Small circles show toroidal location of density are available for all shots, and for some there coils in high bandwidth array, green measure were also measurements of the toroidal rotation ICE on velocity and ion temperature profiles. NSTX(-U) has been observed in plasmas with central



Outer black circle is approximate radius of vacuum vessel on which Mirnov coils are vertical magnetic fluctuations, magenta measure toroidal fluctuations. Red circle shows toroidal location of small vertical array of five coils.

density up to $\approx 4 \times 10^{13}$ /cm³, but ICE is uncommon at densities greater than $\approx 2 \times 10^{13}$ /cm³. With a few exceptions, the plasmas were in L-mode during the ion cyclotron emission period.

The ICE is probably suppressed at higher densities; higher density also appears to be correlated with a broadening of the toroidal rotation profile. The higher density will tend to shorten the fast-ion slowing down time and broaden the fast-ion deposition profile, potentially smoothing the phase-space gradients which could be driving the mode. The higher density could also increase the ICE damping on the thermal ion population. The higher density reduces beam shine-through, increasing beam torque to increase the plasma toroidal rotation, particularly in the "locked" edge region. As the ICE frequency can change substantially when the plasma is shifted radially, but the calculated eigenfrequencies are not seen to change, it is deemed unlikely that an eigenfrequency change due to the density increase is responsible for the ICE suppression.

The high frequency Mirnov coil array on NSTX-U was designed for the study of Compressional and Global Alfvén eigenmodes with expected frequencies below approximately 3 MHz. The edge deuterium ion cyclotron frequency is approximately 3.3 MHz in the nominal 5.9 kG plasmas run in the 2016 campaign. The coils are terminated to provide a flat response to about 3

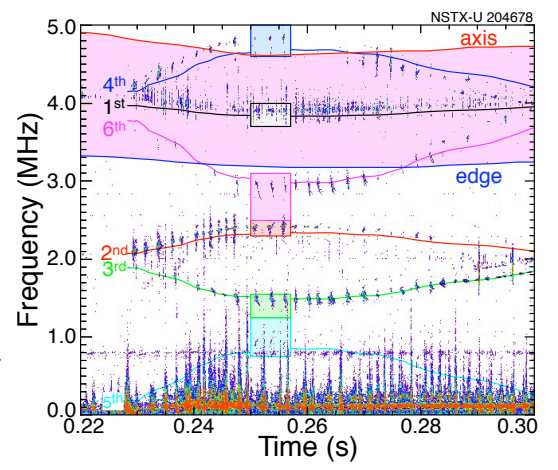
MHz, with an approximate $1/f^2$ fall-off in amplitude response above that frequency. However, to the extent possible, the sensors, terminations, and cabling were kept as similar as possible, thus, it is not unreasonable to attempt mode analysis at frequencies above the nominal bandwidth, albeit with greater uncertainty as to the accuracy of the results. The data acquisition rate was 10 MHz for the data presented here meaning that ICE with frequency above the 2nd or 3rd harmonics is typically aliased. In NSTX-U there is a toroidal array of eleven coils to measure the toroidal mode number and a vertical array of five coils spanning ≈ 65 cm to measure the vertical wavelength on the outboard mid-plane. The toroidal array includes coils which measure the amplitudes and phases of both the toroidal and poloidal magnetic fluctuations (Fig. 2). The Mirnov arrays on NSTX had fewer sensors and the nominal sensor

bandwidth was ≈ 1.8 MHz. The only diagnostic on NSTX(-U), so far, that has detected ICE is the magnetic sensor array.

III. Characteristics of ch-ICE modes

A spectrogram showing ICE and ch-ICE as measured on NSTX-U with $B_{tor} \approx 5.9$ kG is shown in Fig. 3. This figure illustrates some of the complexity of studying the ICE data from the 2016 NSTX-U engineering campaign. The data acquisition rate was

10 MHz and emission near the 2nd and higher Fig. 3. Spectrogram from NSTX-U shot with deuterium cyclotron frequency harmonics is therefore and 2.6 MA plasma current, 5.9 kG toroidal field and 2.6 MW of neutral beam power. The central aliased. Colored curves (labeled "1st" through "6th") density was ≈ 1.4 x 10^{13} /cm³, $T_e \approx 1$ keV. have been added to the spectrogram to identify the Magenta region is f_{ci} between edge and axis.



ICE near the indicated (aliased) Ω_D harmonics. In this figure, the green curve was created by tracking the ICE bursts near the third harmonic. This curve was then used to predict where the aliased emission at other harmonics would be expected. The bursts at other harmonics are typically displaced slightly in frequency, although they roughly align in time, suggesting that the emission near each harmonic is partially independent. When the first harmonic frequency corresponding to the ch-ICE harmonics is calculated, e.g., by dividing the 2nd harmonic frequency by two, the 3^{rd} by three, etc., the resulting frequency is ≈ 100 kHz lower than the fundamental emission (black curve just below the fundamental ICE bursts in Fig. 3).

Sections of the spectrogram, indicated by the shaded boxes in Fig. 3 at ≈ 0.25 s, are expanded in Fig. 4. Each of these expanded spectrograms corresponding to the 2nd through 6th harmonics contains three bursts of ch-ICE. This example is unusual in that chirping ICE is seen at all of the deuterium harmonics from the 2nd to the 6th (Figs. 4a - 4e). No example of ch-ICE has been

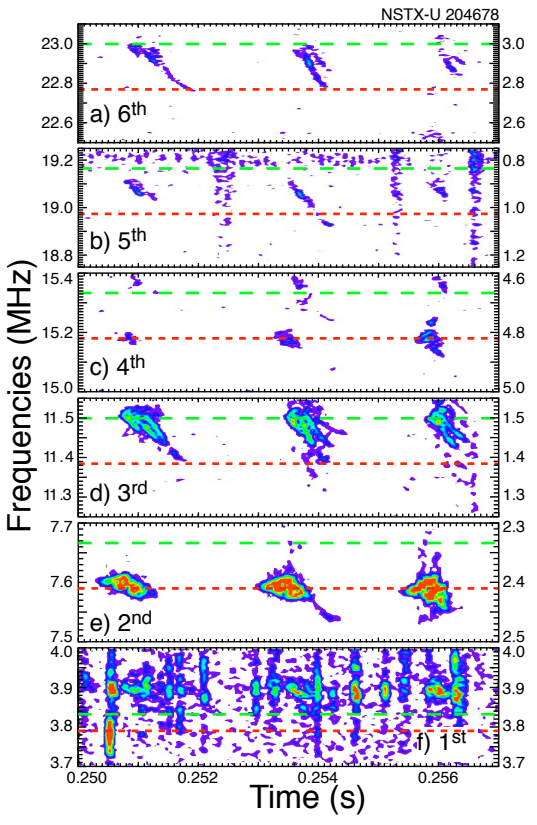
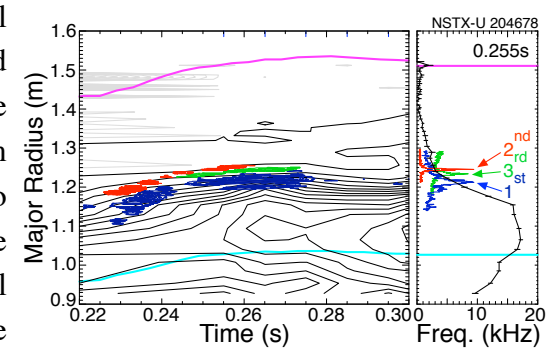


Fig. 4. Expanded sections of the spectrogram aliased, with the original aliased frequency ions assumed to have excited it. ranges on right. The red dashed line shows harmonics of $\Omega_D \approx 3.83$ MHz.

parallel wavelength of the ICE and the parallel velocity of the energetic fast ions. For higher field tokamaks such as TFTR, JT-60U and JET where the estimates of the Doppler correction are much less than the cyclotron frequency, it is not unreasonable to neglect this Doppler correction when mapping the ICE location, particularly since the parallel wavelengths are not typically measured. On the smaller NSTX where the toroidal field is substantially Fig. 5. a) Contours of toroidal rotation frequency lower and the beam energies are comparable, this (black) with mapped ICE spectra overlaid (blue assumption is more problematic. discussed in more detail below where estimates of the curves show the magnetic axis and plasma edge, potential range of the Doppler correction will be respectively b) rotation profile and fluctuation made. In Fig. 5 we neglect the potential Doppler spectra mapped to major radius at indicated time.

found at a frequency corresponding to the fundamental Ω_D . While the timing of the bursts of ch-ICE at the harmonics is clearly correlated, the bursts do not align exactly in time, nor is the spectral structure of the bursts the same for all bursts. This suggests that while there is come coupling between the ch-ICE near each deuterium harmonic, the emission at each harmonic is partially independent. The fundamental ICE harmonic is at about 3.9 MHz (Fig. 4f), but the ICE at higher harmonics is seen at multiples of ≈3.79 MHz (red dashed lines) and multiples of ≈3.83 MHz (green dashed lines). Note that both the red-dashed and green-dashed lines lie below the fundamental ICE frequency in Fig. 4f. These frequencies are also substantially higher than the corresponding harmonics of the edge Ω_D , and thus also map to locations deeper in the plasma.

The spatial origin of the ICE is usually assumed to be from Fig. 3. The figure labeled "1st" shows the near where the observed fundamental ICE frequency normal ICE. The frequency axis have been de- matches the local cyclotron frequency of the energetic However, the harmonics of $\Omega_D \approx 3.79$ MHz, the green shows mapping should also account for the Doppler shift from the cyclotron frequency which depends on the



This will be fundamental ICE, red is ch-ICE near $2\Omega_D$, green is ch-ICE near $3\Omega_D$). The cyan and magenta

frequency corrections and time-dependently map the ICE spectra to the radial profiles of the relevant harmonics of Ω_D . Figure 5a shows toroidal rotation frequency contours (black) with the overlaid, and mapped spectrograms showing the fundamental ICE (blue contours), and the 2nd and 3rd harmonic ch-ICE (red and green, respectively). Figure 5b shows the radial profile of the plasma toroidal rotation and the ICE/ch-ICE spectra at ≈ 0.255 s. The radial profiles of Ω_D are calculated using the local mod(B). As was previously reported [25], the fundamental ICE frequency maps to the bottom of a strong radial gradient in the toroidal rotation. The ch-ICE corresponding to higher Ω_D harmonics maps locations roughly 2 cm to 3 cm farther out in major radius. The ICE frequencies increase and decrease as the plasma is moved radially into higher and lower magnetic field regions (the magenta and cyan curves show the plasma edge and magnetic axis, respectively). The frequency or spatial shift between ICE and ch-ICE could represent a different Doppler frequency correction, or a different spatial origin for the ch-ICE.

It was previously shown that the measured ICE frequency on NSTX(-U) did not have an Alfvénic dependence on density [25]. A similar lack of density scaling has previously been reported on the conventional aspect ratio tokamak TUMAN-3M [19] and in the Large Helical Device (LHD) stellarator [15]. This challenges the theory that ICE is through Alfvén waves, which form eigenmodes with well defined frequencies in the low field NSTX(-U) device. In NSTX-U the lack of ICE frequency scaling with density was determined by showing that the ICE frequency rose during a period when the plasma density roughly doubled. A similar example for ch-ICE is shown in Fig. 6a where the frequency of the ch-ICE emission is

increasing in response to a small inward shift of the plasma. In Fig. 6b the time-smoothed and mapped spectrogram showing ch-ICE (red) is overlaid on contours of the electron density (black). After ≈ 0.215 s the density in the outer plasma region begins to increase, indicating an H-mode transition. This can be seen more clearly in Fig. 6c where profiles of the density at the indicated times are shown. The cyan curve in Fig. 6b shows the radius of the magnetic-axis, the magenta shows the plasma edge. While the density remains largely unchanged in the core region (R < 1.23m), the edge density increases substantially. Calculations of the time evolution of the frequency of compressional Alfvén eigenmodes predict that the ch-ICE frequency, if it (de-aliased), b) ch-ICE spectra overlaid on was an Alfvénic eigenmode, should have dropped by density contours as in Fig. 5, c) profiles of $\approx 7\%~(\approx 500~kHz)$ in response to the increase in edge electron density at indicated times.

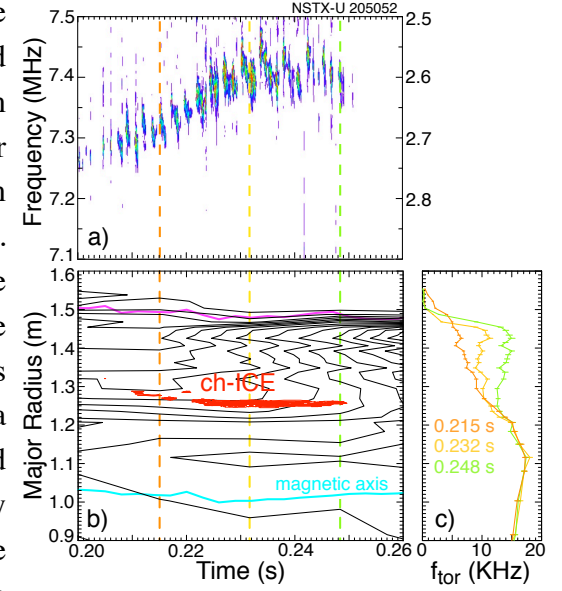


Fig. 6. a) Spectrogram showing ch-ICE bursts

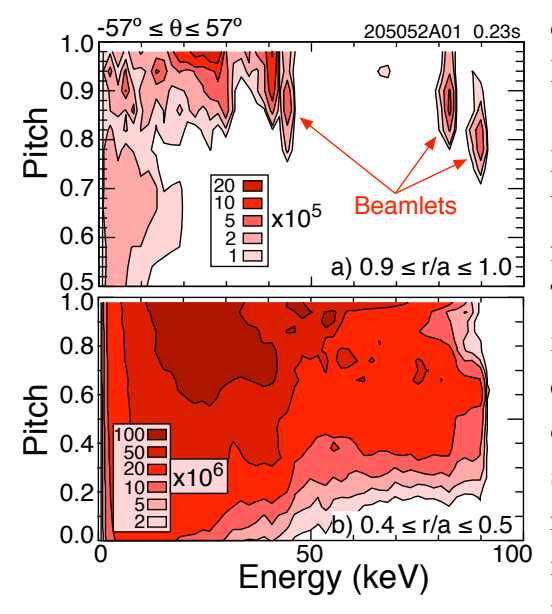


Fig. 7. Deuterium beam ion distribution functions for the ICE seen in Fig. 6. a) narrow function is largely relaxed deeper in plasma.

density between 0.215s and 0.248s. Instead the ch-ICE frequency increased by $\approx 80 \text{ kHz}$.

In conventional tokamaks, the ICE is generally believed to be excited by strong bump-on-tails in the fast-ion distribution at the plasma outboard-edge [9]. The bump-on-tails are formed by barely-trapped fast ions whose orbits pass through the plasma outboard-As this fast-ion population slows down, the orbits contract inwards, away from the plasma edge, so these edge bump-on-tails persist, i.e., they don't relax to a classic slowing-down distribution. measured ICE frequencies on conventional tokamaks, with a few exceptions, were in good agreement with the cyclotron frequency of super-thermal ion bumps-on-tail near plasma edge, b) distribution populations in the plasma edge, supporting this model.

The ICE on NSTX is believed to be driven by some part of the fast beam-ion population. There are, of course, non-thermal populations of fusion products in these plasmas (1 MeV Tritons, 0.8 MeV He³ and 3 MeV protons), however these populations are roughly 2.2 x 10⁶ smaller than the beam-ion population [25]. Figure 7 shows the unperturbed deuterium beam ion distribution as calculated with TRANSP and NUBEAM for a typical NSTX-U plasma where ch-ICE and ICE were seen (this TRANSP run from 2017 pre-dates the current TRANSP version-tracking system). Co-moving fast-ion beamlets are seen in Fig. 7a near the plasma edge at the full and half energies of the beam sources (beam injection energies of 90 keV and 83 keV). The ch-ICE and ICE waves are both propagating counter to the beam-ions, thus a direct Landau resonance is not possible. The fast-ion distribution for the normalized minor radius 0.4 < r/a < 0.45, or in the vicinity of 1.25 m < R < 1.28 m, is shown in Fig. 7b. This location is where the local deuterium cyclotron frequency matches the (ch-)ICE frequencies for this shot. The bump-on-tails are mostly relaxed, leaving only the gradients normally present in a slowing-down distribution to drive the instability. Waves excited through a Doppler-shifted cyclotron resonance can extract energy from other gradients, for example, radial gradients of the population of resonant fast ions.

IV. Bursting and chirping of ch-ICE modes

This new type of ch-ICE has strong bursts with durations of order 1 ms and frequency chirps spanning up to ≈ 200 kHz. The burst spacing was typically 1 to 3 ms. Spectrograms showing

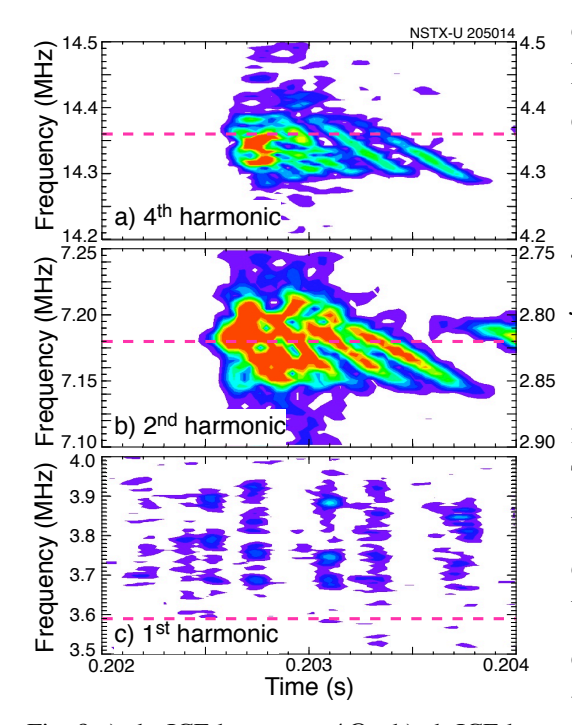


Fig. 8 a) ch- ICE burst near $4\Omega_D$, b) ch-ICE burst near the $2\Omega_D$, and c) spectrogram showing ICE near Ω_D . (Dashed magenta lines are equally spaced in frequency.)

classic hole-clump frequency evolution [53,54] with chirps in both directions. The simultaneous up-down chirps rule out the possibility that the frequency chirps are the result of changes in the toroidal rotation or other equilibrium parameters [24, 28, 29] as the wave chirps both upwards and downwards, simultaneously. The up-down chirping cases resemble the chirping of the (shear) Global Alfvén eigenmodes (GAE) seen in NSTX [55]. Figure 9 compares spectrograms of a GAE burst from NSTX (Fig. 9a) and from a ch-ICE burst in NSTX-U (Fig. 9b). The bursts last a similar period of time, but the frequency range of the ch-ICE chirp is significantly less than that of the GAE. The linear growth rates for the modes have been estimated based on the frequency evolution in accordance with Eq. 52 The red curve (a) and the black curve (b) show

details of a burst of ch-ICE at the $2^{\rm nd}$ and $4^{\rm th}$ Ω_D harmonics are shown in Figs. 8a and 8b. For comparison the ICE bursts near the 1st harmonic are shown in Fig. 8c. As stated above, the 1st harmonic bursts are shorter and uncorrelated with the 2nd and 4th harmonic bursts. The 4th harmonic bursts are not just a non-linear beating of the 2nd harmonic, which would have resulted in a more complex burst structure including mixing between the different frequency components in the 2nd harmonic burst. The bursts are most commonly down-chirping, but up-chirping bursts and bursts that chirp in both directions have been seen. As is seen in Fig. 8, the bursts often consist of several sequential downchirping modes. In Fig. 8b it can be seen that two or three distinct chirping modes can be present at the same time.

The ch-ICE chirps are commonly uni-directional, either up or down in frequency, as in Figs. 8b and 8c, but chirps have been seen which show the

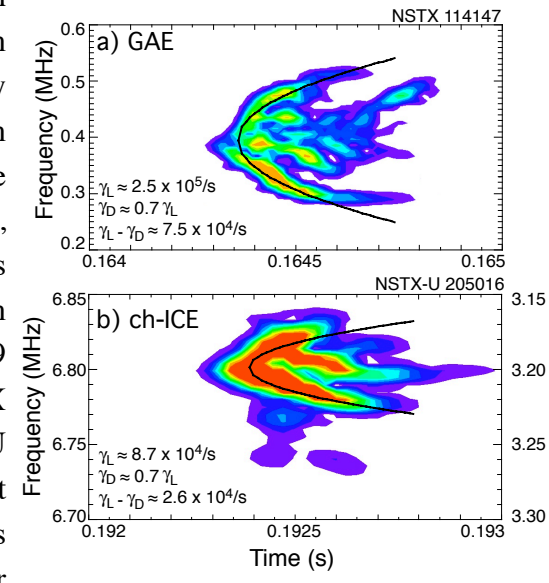


Fig. 9. a) spectrogram of GAE burst on NSTX, b) spectrogram of ch-ICE burst seen on NSTX-U. in Ref. 54, $\delta\omega(t)=\pm~0.441~\gamma_L(\gamma_d~t)^{1/2}$. Here $\delta\omega(t)$ is the predicted frequency evolution assuming the the time-dependent change in frequency, γ_L is the growth and damping rates as indicated.

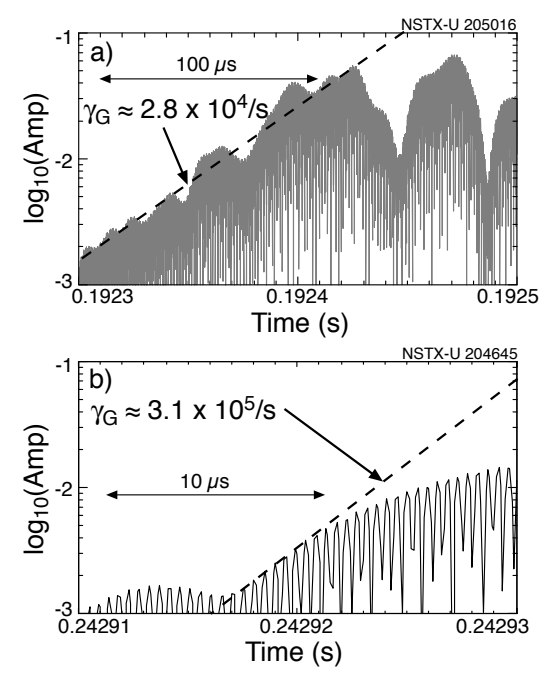


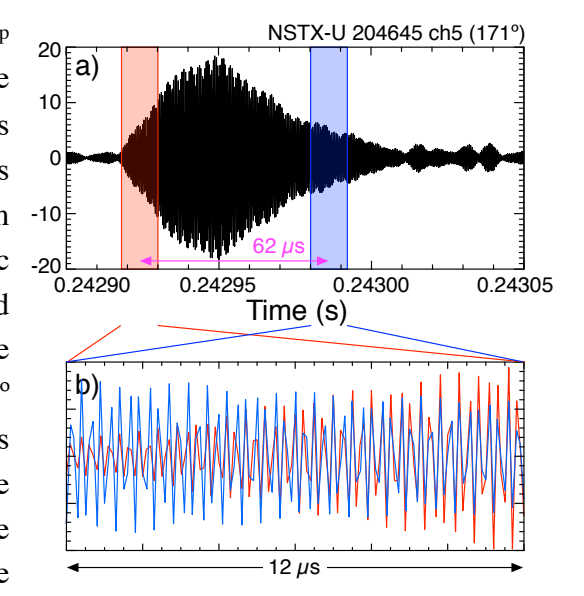
Fig. 10. Graph of the absolute value of the frequencies. magnetic fluctuations a) for the ch-ICE burst shown in Fig. 9b, digitally filtered between 3.15 1st harmonic of Ω_D .

MHz and 3.3 MHz, b) for a burst of ICE near the Chirping of the fundamental ICE bursts has not been seen. The expected range of the frequency chirp can be estimated by using the same formula, but now to predict the chirp rate from the growth rate.

The ICE near Ω_D shown in Fig. 10b has an estimated growth rate of $\approx 3.1 \times 10^{5}$ /s, which is approximately ten times the estimated growth rate of the 2nd harmonic ch-ICE burst growth rate

of $\approx 2.8 \times 10^4$ /s. With the same assumption that γ_{damp} ≈ 0.7 γ_{drive} , the formula then predicts that the frequency should chirp by ≈ 500 kHz over the 62 μ s between the red and blue regions in Fig. 11a, that is from the beginning to the end of the burst shown in Figure 11b overlays the magnetic Fig. 10b. fluctuation traces from the beginning (red) and end (blue) of the ICE burst. As can be seen, the relative phase shift between the two signals is less than 90° over the 45 periods shown in Fig. 11b. corresponds to a change in frequency between the beginning and end of < 0.5%, or < 20 kHz. model in Ref. 53 predicts that the range of the frequency chirp will decrease as the ratio of the Fig. 11. a) Digitally filtered burst of ICE near the damping to linear drive decreases, although the relation is very non-linear. It is necessary to set γ_{damp} / (red) and end (blue) of the ICE burst in a).

linear drive, γ_d is the damping rate and it has been assumed that $\gamma_d \approx 0.7 \gamma_L.$ The equation predicts an initial mode growth rate in reasonable agreement with the amplitude growth of the ch-ICE burst as shown in Fig. 10a, where the initial growth rate of the mode is estimated from the exponential increase in magnetic fluctuation amplitude. For comparison, the growth rate for a burst of ICE at the fundamental Ω_D is shown in Fig. 10b. There is a difference of a factor of ten in the time range between the figures and a corresponding factor of ten larger growth rate for the fundamental ICE. The ch-ICE growth and damping rates are relatively small, $\gamma_{\text{damp}}/\omega_{ICE} \approx 0.14\%$ (using the estimate for the linear damping) and so the waves should form eigenmodes with well defined



1st harmonic of Ω_D (same burst as was shown in Fig. 9b), b) magnetic fluctuations from beginning

 $\gamma_{drive} \approx 0.04$ (the formula is probably not valid for such a low damping rate) to get a frequency chirp as small as 20 kHz. The lack of visible chirping for the normal ICE suggests that there is a major difference between the instability physics of the ch-ICE and regular ICE.

Toroidal and Global Alfvén eigenmode avalanches [56, 57] often temporarily suppress ICE and ch-ICE. This contrasts with previous observations where it was concluded that TAE bursts transported fast ions to the plasma edge which triggered ICE [9, 15] and provides further evidence that the ICE on NSTX is resonantly driven by the fast ion population located deeper in the plasma, where the TAE and GAE are localized. Figure 12a is a spectrogram showing ch-ICE bursts near 2 Ω_D , Fig. 12b shows ICE dashed lines indicate the times of peak TAE amplitude. bursts near Ω_D and Fig. 12c is a spectrogram b) spectrogram of bursting ICE near Ω_D . Following the showing TAE avalanches. The vertical dashed TAE amplitude peaks, the amplitude of the ICE bursts is lines overlaid on each spectrogram indicate the $\frac{1644624}{aliased}$, $\frac{2}{2}$, $\frac{2}{2}$ Again, there are quiet periods time of peak TAE amplitude (TAE amplitude is following the peaks in TAE amplitude. indicated by the black curve in Fig 12c). The

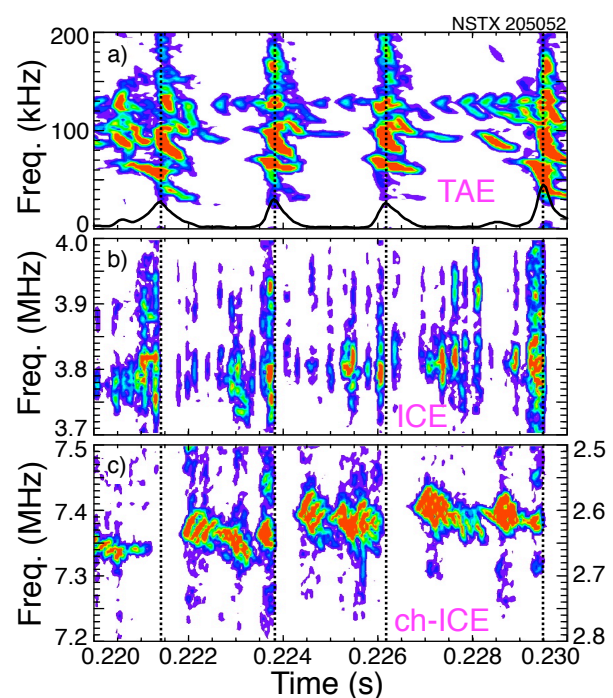


Fig. 12. a) Spectrogram showing TAE avalanches, the black curve is the rms amplitude (a.u.). The vertical reduced, c) spectrogram showing ch-ICE bursts ("de-

correlation isn't strong, but following the peak in TAE amplitude the ICE bursts are weaker and there is a short period where the ch-ICE bursts are absent.

V. Measurement of mode numbers, wavelengths.

The toroidal mode number of the ICE is measured with a toroidal array of eight Mirnov coils oriented to measure the poloidal component of the magnetic fluctuations on the outboard midplane and three oriented to measure toroidal magnetic fluctuations. The approximate toroidal locations of the coils are shown in Fig. 2 with the green circles indicating the location of coils oriented to measure poloidal magnetic fluctuations and the magenta circles indicating the location of coils oriented to measure toroidal magnetic fluctuations. The analysis of mode numbers is done by using Fourier transforms to determine the relative phase between local measurements of the magnetic fluctuations of a given frequency. The relative phase variations are then automatically fit with toroidal mode numbers from n = -14 to n = +14, and the best fits are identified. The range $-14 \le n \le 14$ covers the typical range of toroidal mode numbers found

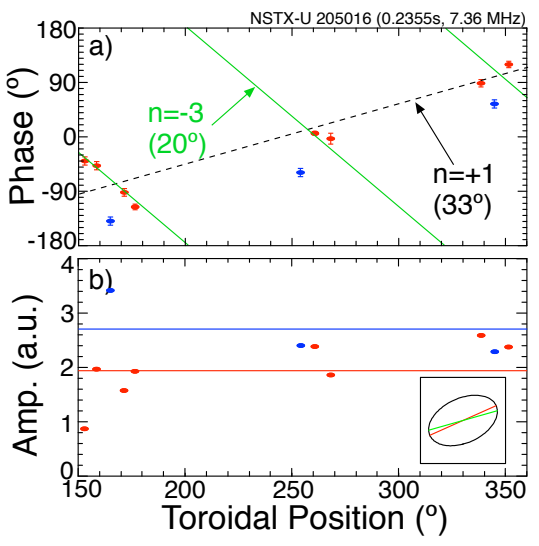


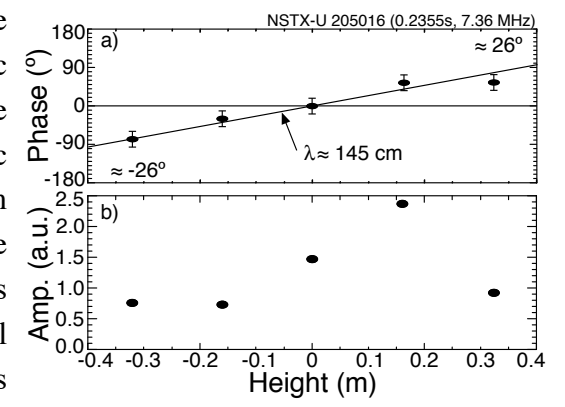
Fig. 13. a) Relative phases of the poloidal magnetic fluctuations vs. toroidal position, green amplitudes. Red points represent poloidal showing compressional polarization.

on NSTX(-U), but fits to higher n's can also be done. The edge polarization of the magnetic fluctuations (from compressional to shear) is calculated from the relative amplitudes and phases of the toroidal magnetic fluctuations relative to the poloidal (vertical) magnetic fluctuations.

Examples illustrating the fitting algorithm for individual points are shown in Figs. 13 and 14. The measured relative phases of the poloidal magnetic fluctuations are shown vs. toroidal position in Fig. 13a. As noted above, the coils are in three groups roughly 90° apart. The solid green line shows the best fit with a standard deviation of 20° to the phase line shows fit to n=-3 with a standard deviation of variation for n=-3 (ctr-propagating). However, as 20°, dashed black line shows fit to n=+1 with the groups of sensors are separated toroidally by standard deviation of 33°, b) fluctuation roughly 90° , the fit to a co-propagating n = 1 mode magnetic fluctuations, blue point are toroidal (black dashed line) is nearly as good with a standard magnetic fluctuations. Inset in b) is a lissajous deviation of 33°. In effect, the discrete toroidal array is susceptible to spatial aliasing in mode number

identification between n and $n \pm 4$. The best fit in this example is determined largely by the group of coils between 150° and 180°. The standard deviation calculation, used to identify the best fit, is weighted by the uncertainty in the phase determination (error bars on each phase point). As a result, for weak or noisy signals with large phase uncertainties, this array can have difficulty resolving the best fit between n and $n \pm 4$. The error bars reflect the signal-to-noise level and don't account for systematic phase errors. In Fig. 13b is shown the amplitude data in a

similar format. The solid red curve shows the average amplitude of the poloidal (vertical) magnetic © 90 average amplitude of the toroidal magnetic fluctuations (with large scatter) Fig. 13b shows a composite Lissajous using the average vertical and toroidal fluctuation amplitudes and the average phase difference between the toroidal and poloidal magnetic fluctuations. The Lissajous trace demonstrates that the polarization of the Fig. 14. a) Relative phases of the poloidal magnetic fluctuations is roughly compressional magnetic fluctuations vs. vertical position on (parallel to the equilibrium field) in the plasma edge.



outboard mid-plane, b) fluctuation amplitudes.

Measurement of the poloidal mode number in a strongly shaped, diverted and low aspect ratio plasma is much more difficult than measuring the toroidal mode number, both in terms of the required diagnostic access as well as interpretation of the measurements due to the poloidal distortion and/or coupling of eigenmodes. In that context, there is some very limited data on the poloidal mode structure of the ICE on NSTX-U as shown in Fig. 14. There is an array of five coils spanning a vertical range of \approx 64 cm, centered on the outboard midplane. While this limited array can't measure the poloidal mode number, it can measure the direction of propagation and a local poloidal wavelength on the outboard midplane.

Figure 14a shows the relative phase, now vs. height relative to the outboard midplane. The best fit to the relative phases corresponds to a vertical (or poloidal) wavelength of ≈ 145 cm on the outboard midplane at the radius of the vacuum vessel wall. Curiously, the inferred poloidal propagation direction is co-parallel to the beam ions, that is, the mode structure has the opposite helicity of the equilibrium magnetic field. In the cylindrical approximation a wavelength of 145 cm would be equivalent to an effective cylindrical poloidal mode number of $m_{eff} \approx 2.7$. (It should be noted that the poloidal array is evenly spaced, and thus subject to spatial aliasing, albeit to very high m's.) Reasonable fits are found for both $m_{eff} = +30$ and $m_{eff} = -24$, however, in either case the resulting k_{ll} would be quite large and the expected Doppler resonant frequency correction would be $O(\omega_{ci})$. A short wavelength would also imply significant attenuation between the plasma edge and the location of the sensor coils. While this may not be a sufficient

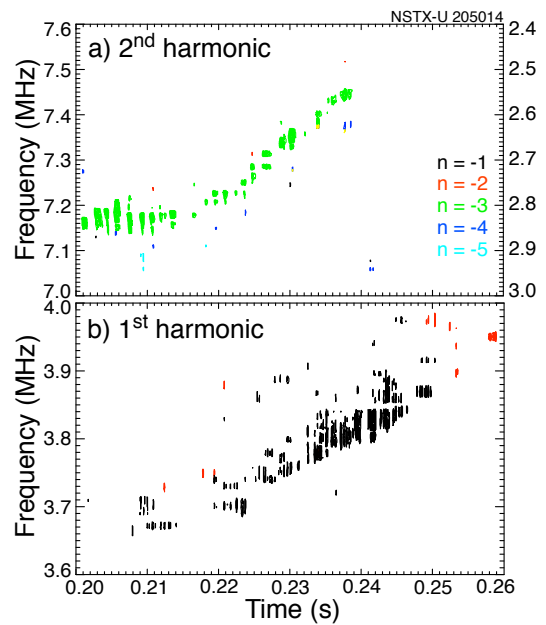


Fig. 15. a) Spectrogram shows best fit toroidal mode numbers for the fundamental ICE bursts.

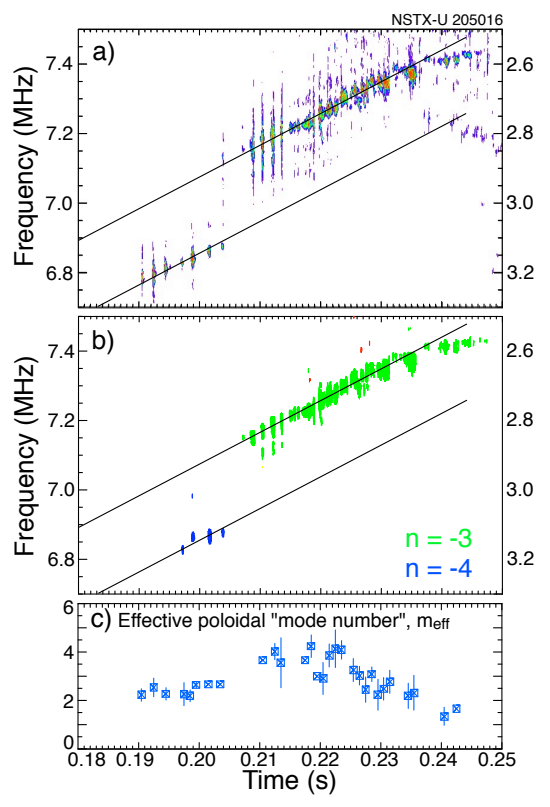
argument to exclude the possibility of very short _{2.5} poloidal wavelengths, it does mean that there would be no reason to expect that ICE frequency harmonics would be separated by ω_{ci} , nor that the ICE frequency 2.8 would be near the deuterium cyclotron frequency. Thus, we consider the short wavelength, high m, fits 3.0 an unlikely possibility.

Analysis of the ICE bursts from many NSTX-U shots have found that the 1st harmonic ICE is typically best fit with a toroidal mode number of n = -1 (negative meaning counter-propagating) and in cases where the 1st harmonic ICE frequency has a split peak, the higher frequency band typically has n = 0. The ch-ICE 2nd harmonic bursts, as seen in previous figures, mode numbers for ch-ICE, b) best fit toroidal are also typically counter-propagating, with n = -3. However, in a couple of shots the best fit was to a copropagating n = +1 mode, and good fits to n = -4 were found in some shots.

The algorithm described above can be adapted for use in a code which automatically finds amplitude peaks in the frequency spectra and finds the best fit to each peak. A threshold for the goodness of fit is used to exclude fits to noise and the resulting list of times, frequencies and mode numbers is used to color-code the contours of a spectrogram. In Fig. 15a is shown an example of such an analysis as applied a sequence of strong 2nd harmonic ch-ICE bursts. The best fits are predominantly n = -3, indicating propagation counter to the plasma current or beam injection direction, that is in the electron diamagnetic drift direction. The measured mode frequency is shown on the right of the figure, and the de-aliased frequency scale on the left. Fig. 15b shows a similar spectrogram for the fundamental ICE harmonic. (Where necessary, the mode numbers have been corrected to account for aliasing.) The modes are again counter-

propagating but with a dominant toroidal mode number of n = -1. The scattering of points depicting mode numbers that are not n = -3 in Fig. 15a, and not n = -1 in Fig. 15b could be spurious fits, or possibly a scattering of ICE bursts with different mode numbers, e.g., in a number of cases, 2nd harmonic ch-ICE was found with best fits of n = -4.

While the best fits for the 1st and 2nd harmonic ICE $\widehat{\mathbb{R}}$ toroidal mode numbers are typically n = -1 and n = -3, toroidal mode numbers are typically n = -1 and n = -3, respectively, other mode numbers $1 \le |n| \le 4$ have also been seen. A spectrogram of the ch-ICE bursts for the same shot as used in Figs. 13 and 14 is shown in Fig. 16a, the toroidal mode number fits are shown in Fig. 16b. The inferred cylindrical poloidal mode numbers, m_{eff} , from this limited range of data are shown in Fig. 16c. The n = -4 ch-ICE bursts have longer poloidal wavelengths (smaller m_{eff}) and shorter toroidal wavelengths than the n = -3 bursts. It is also Fig. 16. a) Spectrogram shows two types of chof interest that the inferred poloidal wavelength for ICE, b) best fit toroidal mode numbers for the chthe n=3 bursts increases (m_{eff} decreases) as the ch- ICE bursts, c) best fit poloidal mode numbers for The n = -4 bursts are ICE frequency increases.



the ch-ICE bursts.

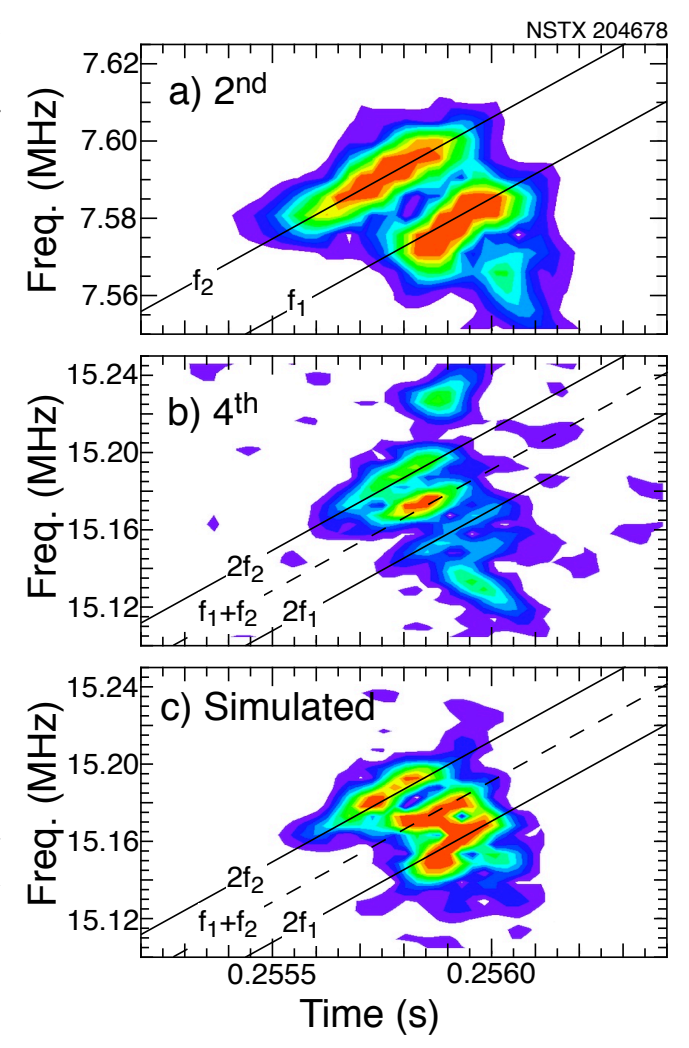
roughly 220 kHz lower in frequency than the n = -3 bursts. For reference, the expected magnitude of the change in resonant frequency should be $\approx \delta n V_{b||}/R$, or 200 kHz to 250 kHz for $\delta n = 1$ assuming other parameters remain constant. Over this time period, the density rise and other parameter changes should have resulted in an approximate 3% drop in the CAE eigenfrequency as opposed to the measured increase of $\approx 5.5\%$. Again, the relative signs of the n and m_{eff} indicate the ICE mode has opposite helicity to the equilibrium magnetic field.

VI. Non-linear coupling of harmonics

The leading theoretical model for the interpretation of ICE predicts that non-linear three-wave coupling between harmonics of ICE emission can transfer energy between harmonics, destabilizing otherwise stable harmonics [41-44]. Experimental evidence for non-linear coupling has been found on KSTAR [23]. Non-linear coupling between ICE and lower frequency shear-

Alfvén waves has been previously reported on NSTX [25]. The data from NSTX(-U) presents an opportunity to search for evidence of non-linear coupling between ICE harmonics. However, the frequencies of the 2nd, 3rd and 4th ICE harmonics are well beyond the nominal bandwidth of the sensors, which raises questions concerning the validity of the relative phase measurements between sensors. Further, the short duration of the bursts and the relatively strong frequency chirping make FFT bi-coherence analysis problematic. With these reservations we find that mode analysis gives reasonable and reproducible results for the 2nd, 3rd and 4th ICE harmonics.

The gain response of the sensors has not been directly calibrated, but has been modeled using a lumped-parameters for the sensors, cabling and terminations. To determine the relative amplitudes of the ICE harmonics, the lumped-parameter model has been used to convert the sensor measurements to absolute magnetic field fluctuation amplitudes for modes with frequencies above the nominal sensor bandwidth.



been used to convert the sensor bursts, the two dominant modes are indicated by the lines measurements to absolute magnetic field labeled f_1 and f_2 , b) spectrogram showing the 2^{nd} harmonic chirping bursts, the two dominant modes are indicated by the lines fluctuation amplitudes for modes with frequencies above the nominal sensor bandwidth.

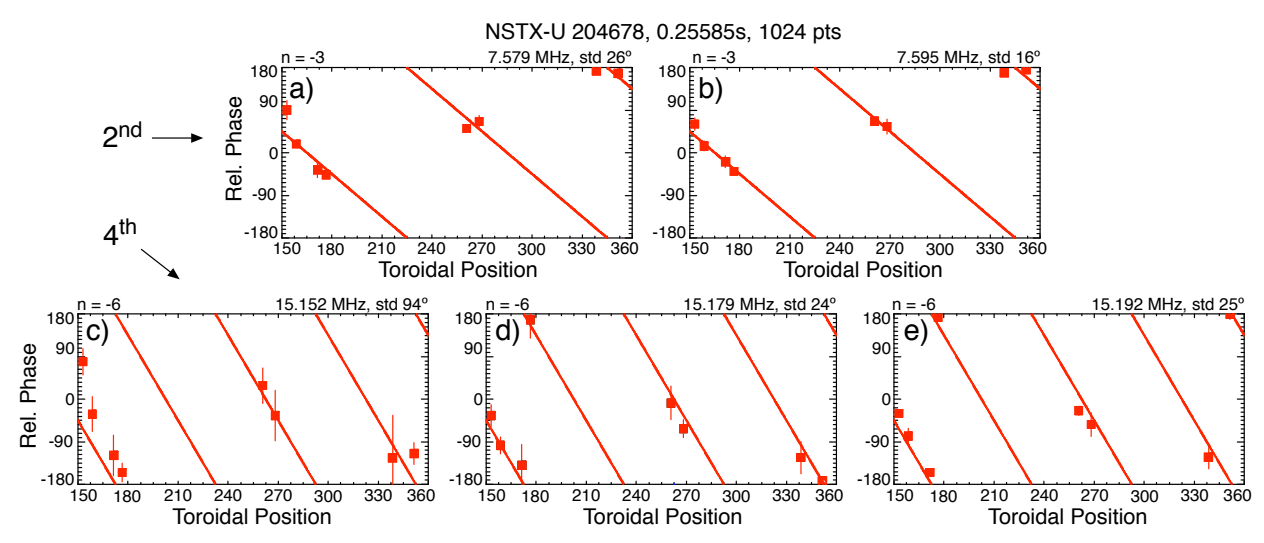


Fig. 18. a) and b) examples of mode analysis of the two dominant modes in Fig. 17a, c) mode analysis of the mode at twice the frequency of the mode in a), d) mode analysis of the mode at the sum of the frequencies of the modes in a) and b), and e) mode analysis of the mode at twice the frequency of the mode in b). The two modes in a) and b) are best fit with toroidal mode numbers of n = -3 (ctr-propagating). The three modes at the sums of the frequencies in a) and b) are best fit with toroidal mode numbers n = -6, that is, the sums of the mode numbers in a) and b). All mode analysis was done at 0.25585s over a 102.4 µs window.

The spectrograms shown in Fig. 17 show evidence of non-linear coupling between the 2nd harmonic bursts and the 4th harmonic bursts. Figure 17a shows a 2nd harmonic chirping ICE burst with two dominant modes, indicated by the solid lines labeled "f₁" and "f₂". Figure 17b

shows the 4th harmonic chirping ICE burst with three clear chirping modes, overlaid by the two solid lines labeled "2f₁" and "2f₂" and the dashed line labeled " f_1+f_2 ". The curves labeled " $2f_1$ " and " $2f_2$ " are at twice the frequencies of the corresponding curves labeled "f₁" and "f₂" in Fig. 17a. Thus, the three individual modes in the 4th harmonic burst have frequencies that are sums of the frequencies of the two dominant modes in the second harmonic bursts. It is important to note that this evidence of non-linear coupling is not seen for all examples with 2nd and 4th harmonic bursts, for example in Fig. 8.

Figure 17c was produced by using the complex Fourier transform of the aliased data to create a spectrum extending to four times the original Nyquist frequency, with the ch-ICE harmonics now at their 7.7 MHz), c) 3rd harmonic (11.3 - 11.6 MHz), d) un-aliased frequencies. This spectrum was filtered to 4th harmonic (15.1 - 15.3 MHz).

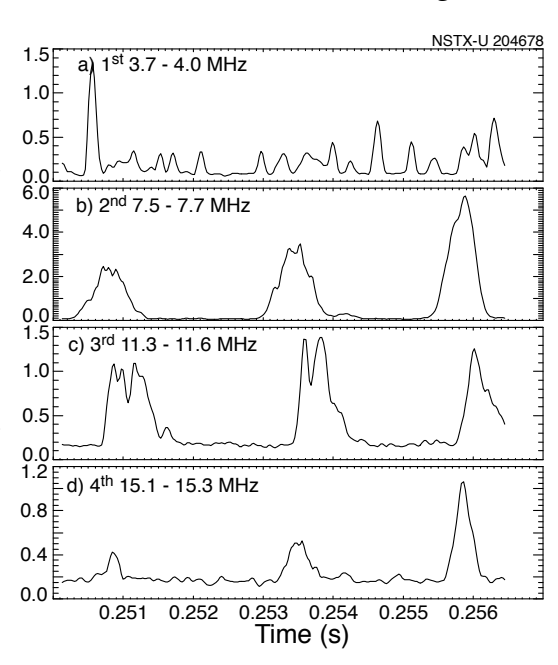


Fig. 19 rms fluctuation amplitudes for a) 1st harmonic (3.7 - 4.0 MHz), b) 2nd harmonic (7.5 -

retain only the 1st and 2nd harmonic ICE and inverted to create a time-trace of fluctuations with an effective acquisition rate of 40 MHz, four times the original acquisition rate. The time-trace was squared to simulate non-linearity and Fig. 1c) is a spectrogram of the resulting simulated signal covering the frequency range of the 4th harmonic burst. As can be seen, the resulting spectrogram appears reasonably similar to the actual measured 4th harmonic burst shown in Fig. 17b.

The non-linear interaction would also put constraints on the wave-vectors of the modes. In this case, we only have good measurements of the toroidal component of the wave-vectors (not the poloidal wave vectors). Figure 18 shows how the wave vectors, *i.e.*, toroidal mode numbers, are related. In these figures the red squares show the phase measurements of the poloidal component of the magnetic field fluctuations and the red lines show the toroidal phase structure with the best fit to the measured phase shifts. The error bars for each point indicate the uncertainty in the

phase measurement and the "std" on the top-right of each figure indicates the root-mean-square, or standard deviation, of the points from the fit lines. The first two figures, Fig. 18a and 18b, show the results of the mode fitting for the two modes seen in Fig. 17a. Both of the modes shown in Fig. 17a are best-fit with an n = -3 mode (here the convention is that negative mode numbers indicate wave propagation counter to the plasma current and beam injection directions). All three of the dominant modes in the 4th harmonic burst are best-fit with n = -6 and are shown in Figs. 18c - 18e. The frequencies for which the fits were done are shown at the top of the figures. The frequency analyzed in Fig. 18c is twice the frequency as that used in Fig. 18a, the frequency in Fig. 18d is the sum of the frequencies from Figs. 18a and 18b and the frequency used in Fig. 18e is twice the frequency from Fig. 18c. (The frequencies are from discrete FFTs with a frequency resolution of \approx 10kHz.) Thus, the dominant modes in Fig. 17a and 17b satisfy the constraints on wave-vectors and frequencies for 3-wave coupling.

The evidence for three-wave coupling between the 1st, 2^{nd} and 3^{rd} harmonics is less clear, but the

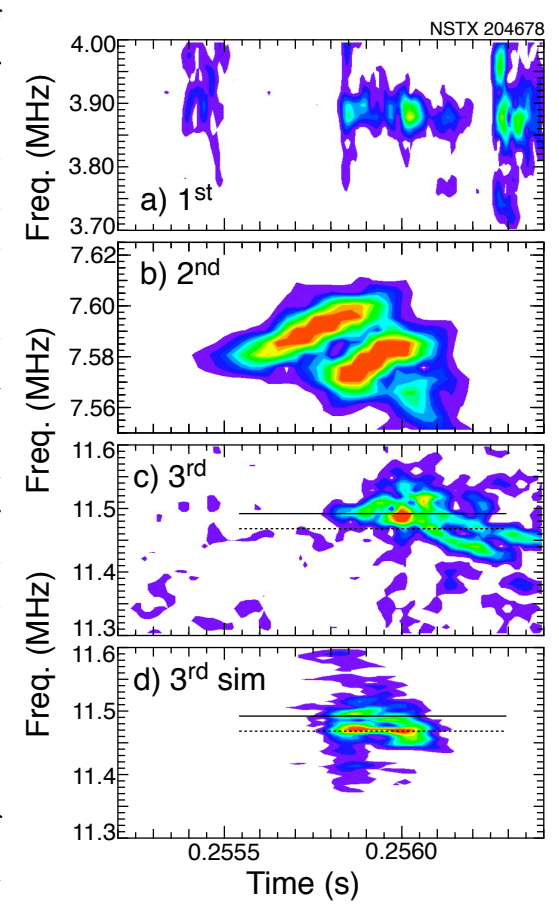


Fig. 20. Spectrograms showing a) fundamental ICE, b) 2^{nd} harmonic ch-ICE, c) 3^{rd} harmonic ch-ICE and d) simulated non-linear 1st and 2nd harmonic interactions at the 3^{rd} harmonic frequency.

frequency and mode number analysis suggest that the data may be consistent with a non-linear coupling model. The fundamental ICE harmonic is weaker than the higher harmonic bursts and the bursts are shorter than are seen for the 2nd and 3rd harmonics. Figure 19 shows the rootmean-square (rms) fluctuation levels for the ICE harmonics. Figure 19a shows the amplitude of the 1st harmonic ICE, filtered over the frequency range from 3.7 MHz to 4.0 MHz. The 1st harmonic ICE has shorter, weaker, bursts that than the higher harmonics. The 2nd and 4th harmonic bursts, Figs. 19b and 19d, show similar shapes in time and the amplitudes of the three 2nd and 4th harmonic bursts are roughly proportional, not what would be expected for a simple non-linear coupling. The 3rd harmonic bursts, Fig. 19c, begin roughly near the peak of the 2nd harmonic bursts, possibly consistent with the model that the 3rd harmonic burst is excited nonlinearly by energy transfer from the 2nd harmonic burst.

The non-linear coupling can be modeled for the 1st, 2nd and 3rd harmonics in the same manner as for the 2nd and 4th harmonics. The spectrograms shown in Fig. 20 don't show as obvious a nonlinear coupling as for the 2nd and 4th harmonics. Figure 20a shows a spectrogram of the 1st harmonic bursts, which mostly overlap in time with the 2nd harmonic burst (Fig. 20b) after

 $\approx 0.2558s$. The third harmonic fluctuations also first appear at about this time, and persist after the end of the 2nd harmonic burst. The frequency chirps for the third harmonic modes are in a downward direction, not upwards like the 2nd harmonic bursts.

Figure 20d shows a simulated non-linear interaction between the 1st and 2nd harmonic bursts, producing fluctuations in the frequency range of the experimental 3rd harmonic burst. The dominant nonlinear 3rd harmonic mode (indicated by the dashed line in Figs. 20c and d) doesn't seem to correspond to an experimentally observed mode. However, a weaker non-linear mode (solid black line) does align reasonably well with the onset frequency of the experimental 3rd harmonic burst. Arguably, the downward frequency chirping observed in the experimental data begins after the end of the 2nd harmonic burst.

modes is also consistent with 3-wave coupling. The to the 3rd harmonic burst.

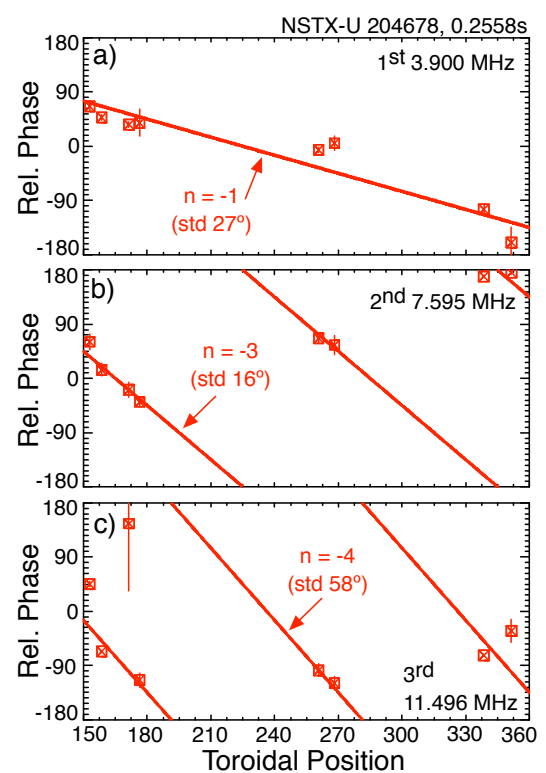


Fig. 21. Toroidal mode number analysis of the 1st, 2nd, and 3rd harmonic ICE bursts. a) best fit of n = -1 to the 1st harmonic burst, b) best fit of the The mode analysis of the 1^{st} , 2^{nd} and 3^{rd} harmonic 2^{nd} harmonic burst to n = -3, c) best fit of n = -4

fits to the 1st, 2nd and 3rd harmonic modes are shown in Fig. 21. The frequency of the 3rd harmonic mode is the sum of the 1st and 2nd harmonic mode frequencies, and the toroidal mode number of the 3rd harmonic mode is also the sum of the toroidal mode numbers of 1st and 2nd modes. These results are also consistent with the type of 3-wave coupling suggested theoretically where the 3-wave interaction acts to trigger a marginally stable mode, which then decays as the energy transfer from the coupled 1st and 2nd harmonic modes drops as the 2nd harmonic chirp amplitude drops.

VII. Discussion of experimental observations

We have presented such characteristics as were possible to measure of the newly discovered chirping ICE, or ch-ICE. The ch-ICE shares some of the characteristics of the non-chirping ICE as were previously reported for NSTX(-U). The ch-ICE is a coherent global mode with a narrow frequency peak, multiple harmonics and the ch-ICE comes in bursts. The burst duration is ≈ 1 ms vs. the shorter $\approx 100~\mu s$ bursts for ICE. The frequency is higher than the edge Ω_D and matches harmonics of Ω_D near an internal transport barrier, as was previously reported for ICE on NSTX(-U). Some features of ch-ICE, and generally for ICE on NSTX(-U), are difficult to reconcile with the standard theoretical interpretation [21-31]. For example, most theoretical interpretations of ICE assume that the frequency is the eigenfrequency of an Alfvénic eigenmode and that the mode is excited through a Doppler-shifted cyclotron resonant drive with a population of non-thermal, barely trapped fast ions near the outboard plasma edge. The ICE is propagating counter to the beam ions and the resonant frequency (ICE frequency) is expected to be Doppler-shifted lower than the edge cyclotron frequency, whereas it is typically significantly higher. The spatial location of the ICE resonant drive remains uncertain. The resonant drive and the eigenmode frequency will be discussed below.

Estimates of the damping and drive for the ch-ICE find that it is weakly damped so the ICE would tend to form eigenmodes. The measured poloidal and toroidal wavelengths of the ICE are smaller than, but comparable in magnitude to, the dimensions of NSTX(-U) plasmas suggesting that the eigenfrequencies would be widely separated and that the eigenmode structures are affected by boundary conditions set by the plasma, plasma facing components, and the vacuum vessel. The relatively long measured wavelengths are roughly consistent with estimates of Compressional Alfvén eigenmode spatial structures for the relatively low field and small physical dimensions of NSTX(-U) plasmas. While the ICE frequency increases linearly with the magnetic field strength, the ICE frequency does not have an Alfvénic scaling with density, an observation that is consistent with recent experiments on TUMAN-3M [18]. The wide spacing of eigenfrequencies means that the non-Alfvénic frequency evolution can not be explained by the ICE evolving through multiple eigenmodes. The chirping of the ch-ICE is a

further difficulty for the eigenmode model, and strongly suggests that ICE has some characteristics of an energetic particle mode (EPM), that is where the frequency is determined by a strong resonant drive from a gradient in the fast-ion distribution.

The correlation of ICE frequency with cyclotron frequency suggests that the ICE is excited through a cyclotron resonance, which, for energetic ions would be Doppler shifted by $k_{II}V_{II}$, where V_{II} is the parallel component of the energetic ion velocity. The ICE and ch-ICE frequencies without beam-ion velocity Doppler corrections match Ω_D , or its harmonics, near a steep radial gradient in the toroidal rotation profile, and/or strong local gradients in the ion temperature profile and electron density profile. This location also often marks the edge of a core region inside of which the electron temperature profile is flat. The strong correlation of the ICE frequency with Ω_D at the transport barrier provides strong evidence that this is the location of the resonant drive for the (ch-)ICE and that there is only a negligible Doppler correction. A small Doppler correction appears inconsistent with the measured ICE wavelengths and the ICE eigenmodes having opposite helicity to the equilibrium magnetic field. In this situation the k_{II} can not approach zero near a resonant rational surface. Conversely, using the Doppler-corrected frequency leaves the spatial origin of the ICE even deeper in the plasma and uncorrelated with any localized plasma feature.

For NSTX(-U) fast ion velocity, V_{II} is positive and for NSTX(-U) ICE k_{II} < 0 which results in a downshift of the ICE frequency from the cyclotron frequency. We can estimate the order of magnitude of this Doppler shift by using some typical parameters. For a deuterium beam with maximum beam-ion energy of 90 keV, the beam-ion speed is $\approx 2.9 \text{ x } 10^6 \text{ m/s}$. The approximate local expression for the parallel wavenumber is $k_{\parallel} \approx (n - mq)/(qR)$. The measurements find n = -3 for the fundamental ch-ICE near the 2nd cyclotron harmonic of deuterium. The poloidal mode number is not measured, but the direction of poloidal propagation indicates that the ch-ICE has opposite helicity to the equilibrium field. From this we can estimate the order of magnitude for k_{ll} as $\approx (\ln |q + m|/qR_{edge}) > 3/R_{edge}$ (n = -3). For NSTX(-U) these assumptions would predict a Doppler-shift frequency correction of ≈ 0.65 MHz (neglecting the contribution from m and using $R_{edge} = 1.5 m$). The Doppler correction to the resonance frequency would shift the resonance location inwards by more than 13 cm, even farther from the plasma edge. For the Doppler frequency correction to be negligible, the parallel beam velocity and/or k_{ll} would need to be much smaller. To make k_{\parallel} smaller would require the helicity of the mode to reverse deeper in the plasma (to match the equilibrium field helicity) which seems unlikely. alternative explanation would be a population of beam ions with small pitch, that is small V_{\parallel}/V . Figure 7b does show that there is such a population, albeit at energies below about 50 keV.

The leading theoretical model for the interpretation of ICE has predicted that non-linear three-wave coupling could be responsible for destabilizing modes at harmonics that are linearly stable. The evidence presented here suggests that non-linear effects are present that result in the non-linear coupling of ICE harmonics and possibly three wave coupling that transiently excites a possibly linearly stable 3rd harmonic. These observations are tempered by the observation that the higher ICE harmonics can be more than three times the data acquisition Nyquist frequency and more than five times the nominal bandwidth of the diagnostic used to make the ICE measurements. These experiments should be revisited with a higher bandwidth system to confirm these preliminary observations.

The suppression of the toroidal rotation in the outer region of the plasma could indicate the presence of error-field induced locked modes, a common problem during the current ramp phase on NSTX(-U). The presence of the error fields, and potentially locked tearing modes, could cause stochastic diffusion of fast ions, particularly the trapped fast ions, that is, those with small V_{\parallel} . The low field of NSTX(-U) means that the threshold for stochastic fast ion loss is also relatively low. An approximate analytic expression for the threshold displacement for stochastic diffusion of trapped ions is given by [58]:

$$\xi_r > R/[2\rho_{fast}q'(\pi nq/\varepsilon)^{3/2}]$$

where ξ_r is the displacement, R is the local major radius, ρ_{fast} is the fast-ion Larmor radius and ε is the local inverse aspect ratio. For a typical ch-ICE case, these equations predict that the stochastic threshold is ≈ 0.5 cm displacement at R ≈ 1.25 m for the 45 keV trapped fast ions. It is then possible that there is significant loss of the trapped fast ions in the region with low toroidal velocity, and possibly a strong radial gradient in these resonant trapped fast ions. This amplitude of radial displacement could be consistent with islands created by error fields.

An alternative explanation is that mode conversion physics might act as a filter on waves excited in the core region by the beam ions, with only waves near harmonics of the thermal ion cyclotron frequency at the mode conversion layer allowed to propagate out [46]. In this case the range of ICE frequencies could be constrained by the width of the mode-conversion layer as the thermal Larmor radius is < 1cm and Doppler corrections would be negligible. In the region outside the mode-conversion layer, the ICE would be ion cyclotron waves (ICW), which propagate perpendicular to the magnetic field, have a short radial wavelength and wouldn't have a narrowly defined frequency. This explanation would have difficulties explaining the chirping ICE, however.

VIII. Summary

We describe a new type of frequency chirping ICE, which we refer to as ch-ICE. This ch-ICE appears as repetitive bursts with duration of ≈ 1 ms, longer than for the typical ICE bursts of $\approx 50~\mu s$ reported previously for NSTX(-U). The chirping resembles that expected for weakly unstable fast particle driven instabilities [45], and the growth rate inferred from the frequency evolution in the chirps is in reasonable agreement with that inferred from direct measurements of the amplitude growth. The lowest observed harmonic of ch-ICE is typically slightly lower than the frequency of the 2^{nd} harmonic of the fundamental ICE. The experimental observations on ICE from NSTX(-U) reported here are more detailed than is generally available from higher field conventional tokamaks, and there is greater variation in the ICE characteristics. The observations presented here, and previously, of ICE in the parameter regime of low-aspect ratio tokamak plasmas challenge the leading theoretical models for non-thermal ion cyclotron emission. Hopefully these measurements, and new measurements with some diagnostic improvements, will help to guide an advance in theory, potentially making ICE diagnostics and approach to measure parameters of the confined fast ion population in future devices.

Acknowledgements

The authors appreciate the support of the NSTX project in the construction and installation of the high-frequency magnetic sensor arrays that made these observations possible. We especially thank the G. Smalley and D. LaBrie for their ingenuity in designing and building the sensing coils used here. This work was supported by US DOE Contract DE-AC02-09CH11466. The digital data for this paper can be found following the links from http://arks.princeton.edu/ark:/88435/dsp018p58pg29j.

Bibliography:

- [1] *Microinstability Limitations of the DCX-1 Energetic Plasma*, J. L. Dunlap, G. R. Haste, C. E. Nielsen, H. Postma, and L. H. Reber, Phys. Fluids **9** (1966) 199.
- [2] Radiation and Ion Energy Distributions of the DCX-1 Plasma, J. L. Dunlap, C.F. Barnett, R.A. Dandi, H. Postma, Nucl. Fusion Supplement, Part 1, p233 (1962).
- [3] Excitation of Ion Cyclotron Harmonic Waves in a Plasma by a Perpendicularly Injected Electron Beam, T. Yamamoto, T. Suito, Journal of the Physical Society of Japan 24 (1968) 953.
- [4] Équipe T.F.R., Nucl. Fusion **18** (1978) 1271.
- [5] High Frequency Emission from TFTR plasmas, G.J. Greene, P.L. Colestock, E.D. Fredrickson, J.C. Hosea, K.M. McGuire, J.R. Wilson, K.M. Young, in Controlled Fusion and Plasma Heating (Proc. 15th Eur. Conf. Dubrovnik, 1988), Vol. 12B, Part I, European Physical Society, Geneva (1988) 107.
- [6] Superthermal Radiation from Fusion Products in JET, Cottrell, G.A., Dendy, R.O., Phys. Rev. Lett. **60** (1988) 33.
- [7] Sawtooth oscillations in ion cyclotron emission from JET, P. Schild, G. A. Cottrell, R. O. Dendy, Nucl. Fusion **29** (1989) 834.
- [8] Measurement of Ion Cyclotron Emission and ICRF-driven waves in TFTR, G. J. Greene and the TFTR Team, in Proceedings of the 17th European Conference on Controlled Fusion and Plasma Heating, Amsterdam, Netherlands, 1990, edited by G. Briffod, A. Nijsen-Vis, and F. C. Schüller (European Physical Society, Petit-Lancy, Switzerland, 1990), Part IV, Vol. 14B, p. 1540.
- [9] Ion Cyclotron Emission Measurements During JET Deuterium-Tritium Experiments, G. A. Cottrell, V. P. Bhatnagar, O. Da Costa, R. O. Dendy, J. Jacquinot, K.G. McClements, D.C. McCune, M.F.F. Nave, P. Smeulders, D.F.H. Start, Nucl. Fusion 33 (1993) 1365.
- [10] Loss of energetic beam ions during TAE instabilities, H.H. Duong, W.W. Heidbrink, E.J. Strait, T.W. Petrie, R. Lee, R.A. Moyer, J.G. Watkins Nucl. Fusion **33** (1993) 749.
- [11] Ion cyclotron emission on the Tokamak Fusion Test Reactor, Cauffman, S., Majeski, R., Rev. Sci. Instrum. **66** (1995) 817.
- [12] Alfvénic Behaviour of Alpha Particle Driven Ion Cyclotron Emission in TFTR, Cauffman, S., Majeski, K.G. McClements, R.O. Dendy, Nucl. Fusion **35** (1995) 1597.
- [13] Observation of spontaneously excited waves in the ion cyclotron frequency range on JT-60U, M. Ichimura, H. Higaki, S. Kakimoto, Y. Yamaguchi, K. Nemoto, M. Katano, M. Ishikawa, S. Moriyama and T. Suzuki, Nucl. Fusion **48** (2008) 035012.
- [14] Observation of Ion Cyclotron Emission Owing to DD Fusion Product H Ions in JT-60U, Shoichi Sato, Makoto Ichimura, Yuusuke Yamaguchi, Makoto Katano, Yasutaka Imai, Tatsuya Murakami, Yuichiro Miyake, Takuro Yokoyama, Shinichi Moriyama, Takayuki Kobayashi, Atsushi Kohima, Koji Shinohara, Yoshiteru Sakamoto, Tsuguhiro Watanabi, Hitoshi Hojo and Tsuyoshi Imai, Plasma and Fusion Research 5 (2010), S2067.

- [15] Measurement of Ion Cyclotron Emissions by Using High-Frequency Magnetic Probes in the LHD, Kenji Saito, Ryuhei Kumazawa, Tetsuo Seki, Hiroshi Kasahara, Goro Nomura, Fujio Shimpo, Hiroe Igami, Mitsutaka Isobe, Kunihiro Ogawa, Kazuo Toi, Masaki Osakabi Masaki Nishiura, Tsuguhiro Watanabi, Satoshi Yamamoto, Makoto Ichimura, Takashi Mutoh, Plasma Science and Technology 15 (2013), 209.
- [16] Alfvén Eigenmode and Energetic Particle Research in JT-60U, H. Kimura, Y. Kusama, M. Saigusa, G.J. Kramer, K. Tobita, M. Nemoto, T. Konkoh, T. Nishitani, O. Da Costa, T. Ozeki, T. Oikawa, S. Moriyama, A. Morioka, G.Y. Fu, C. Z. Cheng, V. I. Afanastev, Nucl. Fusion 38 (1998), 1303.
- [17] *Ion Cyclotron Emission on ASDEX Upgrade*, R. D'Inca, Ph.D thesis, Max Planck Institute for Plasma Physics, 2014.
- [18] Dynamic spectra of radio frequency bursts associated with edge-localized modes, Shekar G Thatipamula, G S Yun, J Leem, H K Park, K W Kim, T Akiyama, S G Lee, Plasma Phys. Control. Fusion **58** (2016) 065003.
- [19] *Ion cyclotron emission in NBI-heated plasmas in the TUMAN-3M tokamak*, L.G. Askinazi, A.A. Belokurov, D.B. Gin, V.A. kornev, S.V. Lebedev, A.E. Shevelev, A.S. Tukachinsky, N.A. Zhubr, Nucl. Fusion **58** (2018) 082003.
- [20] Radio frequency measurements of energetic-particle-driven emission using the ion cyclotron emission diagnostic on the DIII-D tokamak, K. E. Thome, D. C. Pace, R. I. Pinsker, O. Meneghini, C. A. del Castillo, and Y. Zhu, Rev. Sci. Instrum. 89, 10I102 (2018); doi: 10.1063/1.5035561
- [21] High-Frequency Energetic Particle Driven Instabilities and Their Implications for Burning Plasmas, K E Thome, A. Lvovskiy, S. Tang, N.A. Crocker, X.D. Du, W.W. Heidbrink, Y.B. Zhu, D.A. Spong, D.C. Pace, C.A. Paz-Soldan, R.I. Pinsker, C.S. Collins, M.A. Van Zeeland, M.E. Austin, C.A. del Castillo, in 27th IAEA Fusion Energy Conference, Gandhinagar, India, 22–27 October 2018 (IAEA, Vienna), paper EX/P6-29.
- [22] Observations and modelling of ion cyclotron emission observed in JET plasmas using a sub-harmonic arc detection system during ion cyclotron resonance heating, K.G. McClements, A. Brisset, B. Chapman, S.C. Chapman, R.O. Dendy, P. Jacquet, V.G. Kiptily, M. Mantsinen, B.C.G. Reman, Nucl. Fusion **58** (2018) 096020.
- [23] Nonlinear wave interactions generate high-harmonic cyclotron emission from fusion-born protons during a KSTAR ELM crash, B. Chapman, R.O. Dendy, S.C. Chapman, K.G. McClements, G.S. Yun, S.G. Thatipamula, M.H. Kim, Nucl. Fusion **58** (2018) 096027.
- [24] Distinct stages of radio frequency emission at the onset of pedestal collapse in KSTAR H-mode plasmas, M.H. Kim, S.G. Thatipamula, J.E. Lee, M.J. Choi, H.K. Park, T. Akiyama, G.S. Yun, Nucl. Fusion **58** (2018) 096034
- [25] Emission in the ion cyclotron range of frequencies (ICE) on NSTX and NSTX-U, E. D. Fredrickson, N. N. Gorelenkov, R. E. Bell, A. Diallo, B. P. LeBlanc, M. Podestà, and NSTX Team, Phys. Plasmas 26, 032111 (2019); https://doi.org/10.1063/1.5081047

- [26] Central ion cyclotron emission in the DIII-D tokamak, K.E. Thome, D.C. Pace, R.I. Pinsker, M.A. Van Zeeland, W.W. Heidbrink and M.E. Austin, Nucl. Fusion **59** (2019) 086011.
- [27] Ion cyclotron emission driven by deuterium neutral beam injection and core fusion reaction ions in EAST, L. Liu, Xinjun Zhang, Yubao Zhu, Chengming Qin, Yanping Zhao, Shuai Yuan, Yuzhou Mao, Miaohui Li, Kai Zhang, Jian Cheng, Lin Ai, Yan Cheng, Nucl. Fusion **60** (2020) 044002.
- [28] Interpretation of core ion cyclotron emission driven by sub-Alfvénic beam-injected ions via magnetoacoustic cyclotron instability, R. Ochoukov, K.G. McClements, R. Bilato, V. Bobkov, B. Chapman, S.C. Chapman, R.O. Dendy, M. Dreva, H. Faugel, J.-M. Noterdaeme, Nucl. Fusion 59 (2019) 086032.
- [29] Explanation of core ion cyclotron emission from beam-ion heated plasmas in ASDEX Upgrade by the magnetoacoustic cyclotron instability, L. Liu, R. Ochoukov, K. G. McClements, R. O. Dendy, V. V. Bobkov, M. Weiland, R. Bilato, H. Faugel, D. Moseev, M. Salewski, Wei Zhang, Xinjun Zhang, Yubao Zhu, B. Chapman, A. Zalzali, ASDEX Upgrade team and EUROfusion MST team, Nucl. Fusion 61 (2020), 026004.
- [30] Ion Cyclotron Emission Studies: Retrospects and Prospects, N N Gorelenkov, Plasma Phys. Reports 42 (2016) 430.
- [31] Energetic particle-driven compressional Alfvén eigenmodes and prospects for ion cyclotron emission studies in fusion plasmas, N N Gorelenkov, New J. Phys. **18** (2016) 105010.
- [32] R. O. Dendy, C. N. Lashmore-Davies, and K. F. Kam, Phys. Fluids B 4 (1992), 3996.
- [33] The magnetoacoustic cyclotron instability of an extended shell distribution of energetic ions, R. O. Dendy, C. N. Lashmore-Davies, and K. F. Kam, Phys. Fluids B **5** (1993), 1937.
- [34] The excitation of obliquely propagating fast Alfvén waves at fusion ion cyclotron harmonics, R. O. Dendy, C. N. Lashmore-Davies, K. G. McClements, and G. A. Cottrell, Phys. Plasmas 1 (1994), 1918.
- [35] Alfvén Cyclotron Instability and Ion Cyclotron Emission, Gorelenkov, N.N. and Cheng, C.Z., Nucl. Fusion **35** (1995) 1743.
- [36] Excitation of Alfvén cyclotron instability by charged fusion products in tokamaks, N. N. Gorelenkov and C. Z. Cheng, Physics of Plasmas 2 (1995) 1961.
- [37] Interpretation of ion cyclotron emission from sub-Alfvénic fusion products in the Tokamak Fusion Test Reactor, K G McClements, R O Dendy, C N Lashmore-Davier, G A Cottrell, Phys. Plasmas 3 (1996) 543.
- [38] Origin of Superthermal Ion Cyclotron emission in tokamaks, T. Fülöp, Ya. I Kolesnichenko, M Lisak, D Anderson, Nucl. Fusion 37 (1997) 1281.
- [39] Ion cyclotron emission from fusion products and beam ions in the Tokamak Fusion Test Reactor, T. Fülöp, M. Lisak, Nucl. Fusion **38** (1998) 761.
- [40] A mechanism for beam-driven excitation of ion cyclotron harmonic waves in the Tokamak Fusion Test Reactor, R. O. Dendy, K. G. McClements, C. N. Lashmore-Davies, R. Majeski and S. Cauffman, Phys. Plasmas 1 (1994) 3407.

- [41] Particle-in-cell simulations of the magnetoacoustic cyclotron instability of fusion-born alpha-particles in tokamak plasmas, J W S Cook, R O Dendy and S C Chapman, Plasma Phys. Control. Fusion **55** (2013) 065003.
- [42] Linear and nonlinear physics of the magnetoacoustic cyclotron instability of fusion-born ions in relation to ion cyclotron emission, L. Carbajal, R. O. Dendy, S. C. Chapman, and J. W. S. Cook, Phys. Plasmas 21 (2014), 012106.
- [43] Ion cyclotron emission from fusion-born ions in large tokamak plasmas: a brief review from JET and TFTR to ITER, R O Dendy, K G McClements, Plasma Phys. and Control. Fusion **57** (2015) 044002.
- [44] Quantifying Fusion Born Ion Populations in Magnetically Confined Plasmas using Ion Cyclotron Emission, L. Carbajal, R O Dendy S C Chapman, J W S Cook, Phys. Rev. Lett. 118 (2017) 105001.
- [45] Fast particle-driven ion cyclotron emission (ICE) in tokamak plasmas and the case for an ICE diagnostic in ITER, K.G. McClements, R. D'Inca, R.O. Dendy, L. Carbaja, S.C. Chapman, J.W.S. Cook, R.W. Harvey, W.W. Heidbrink and S.D. Pinches, Nucl. Fusion 55 (2015) 043013.
- [46] Ion Bernstein wave heating research, Masayuki Ono, Phys. Fluids **B 5** (1993) 241.
- [47] *Ion cyclotron and spin-flip emissions from fusion products in tokamaks*, V. Arunasalam, G.J. Greene and K.M. Young, Nucl. Fusion **34** (1994) 927.
- [48] *Compressional Alfvén eigenmodes on MAST*, L. C. Appel, T. Fülöp, M. J. Hole, H. M. Smith, S. D. Pinches, R. G. L. Vann and The MAST Team, Plasma Phys. Control. Fusion **50**, 115011 (2008).
- [49] Non-linear modulation of short wavelength compressional Alfvén eigenmodes, E. D. Fredrickson, N. N. Gorelenkov, M. Podesta, A. Bortolon, N. A. Crocker, S. P. Gerhardt, R. E. Bell, A. Diallo, B. LeBlanc, F. M. Levinton, H. Yuh, Phys. of Plasmas 20, 042112 (2013).
- [50] Density perturbation mode structure of high frequency compressional and global Alfvén eigenmodes in the National Spherical Torus Experiment using a novel reflectometer analysis technique, N. A. Crocker, S. Kubota, W. A. Peebles, T. L. Rhodes, E. D. Fredrickson, E. Belova, A. Diallo, B. P. LeBlanc, S. A. Sabbagh, Nucl. Fusion **58** (2018) 016051.
- [51] Overview of NSTX Upgrade initial results and modeling highlights, J. E. Menard, J.P. Allain, D.J. Battaglia, et al., Nucl. Fusion 10 (2017) 102006.
- [52] Scenario development during commissioning operations on the National Spherical Torus Experiment Upgrade, D. J. Battaglia, M.D. Boyer, S. Gerhardt, D. Mueller, C.E. Myers, W. Guttenfelder, J.E. Menard, S.A. Sabbagh, F. Scotti, F. Bedoya, Nucl. Fusion 58 (2018) 046010.

- [53] Spontaneous hole-clump pair creation in weakly unstable plasmas, H. L. Berk, B. N. Breizman, and N. V. Petviashvili, Phys. Lett. A 234, 213 1997.
- [54] Spontaneous hole-clump pair creation, H. L. Berk, B. N. Breizman, J. Candy, M. Pekker, and N. V. Petviashvili, Phys. Plasmas 6 (1999) 3102.
- [55] Collective fast ion instability-induced losses in NSTX, E.D. Fredrickson, R. Bell, D. Darrow, G. Fu, N. Gorelenkov, B. LeBlanc, S. Medley, J. Menard, H. Park, L. Roquemore, S. A. Sabbagh, D. Stutman, K. Tritz, N. Crocker, S. Kubota, W. Peebles, K.C. Lee, F. Levinton, Phys. of Plasmas 13 (2006) p056109.
- [56] Fast-ion energy loss during TAE avalanches in the National Spherical Torus Experiment, E.D. Fredrickson, N.A. Crocker, D.S. Darrow, N.N. Gorelenkov, G.J. Kramer, S. Kubota, M. Podesta, R.B. White, A. Bortolon, S.P. Gerhardt, R.E. Bell, A. Diallo, B. LeBlanc, F.M. Levinton and H. Yuh, Nucl. Fusion 53 (2013) 013006.
- [57] Observation of global Alfvén eigenmode avalanche events on the National Spherical Torus Experiment, E.D. Fredrickson, N.N. Gorelenkov, E. Belova, N.A. Crocker, S. Kubota, G.J. Kramer, B. LeBlanc, R.E. Bell, M. Podesta, H. Yuh and F. Levinton, Nuclear Fusion 52 (2012) 043001.
- [58] Alpha particle confinement in tokamaks, R.B. White and H. E. Mynick, Phys.Fluids B 1 (1989) 980.